RESEARCH ARTICLE

Key Points:
- The Monroe landslide has four major kinematic elements and displays seasonal kinematic changes
- Estimates from mass conservation reveal slide thickening at the longitudinal center near the transition from subsidence to uplift
- The correlation between the landslide rate and the rainfall-modulated pore pressure changes constrains the hydraulic diffusivity

Supporting Information:
- Supporting Information S1

Correspondence to:
X. Hu,
xiehu@berkeley.edu

Mobility, Thickness, and Hydraulic Diffusivity of the Slow-Moving Monroe Landslide in California Revealed by L-Band Satellite Radar Interferometry

Xie Hu[1,2,3] (iD), **Roland Bürgmann[2,3]** (iD), **Zhong Lu[1]** (iD), **Alexander L. Handwerger[4]** (iD), **Teng Wang[5,6]** (iD), and **Runze Miao[3]**

[1]Roy M. Huffington Department of Earth Sciences, Southern Methodist University, Dallas, CA, USA, [2]Berkeley Seismological Laboratory, University of California, Berkeley, CA, USA, [3]Department of Earth and Planetary Science, University of California, Berkeley, CA, USA, [4]Jet Propulsion Laboratory, California Institute of Technology, Pasadena, CA, USA, [5]Earth Observatory of Singapore, Nanyang Technological University, Singapore, [6]Now at School of Earth and Space Sciences, Peking University, Beijing, China

Abstract Active landslides cause fatalities and property losses worldwide. Landslide behaviors can be enigmatic in natural landscapes and therefore require high-quality observations of their kinematics to improve our ability to predict landslide behavior. Here we use geodetic interferometric synthetic aperture radar (InSAR) observations to characterize the geometry and the spatio-temporal deformation of the slow-moving, deep-seated Monroe landslide in northern California between 2007 and 2017. InSAR phase discontinuities show that the landslide is bounded by discrete strike-slip faults at the lateral margins and segregated into distinct kinematic elements by normal and thrust faults. We find that the Monroe landslide has been moving consistently, with a maximum rate of about 0.7 m/year in the narrowest longitudinal center of the transport zone. The thickest landslide mass is estimated to be in a zone located between subsiding and the uplifting kinematic elements at the lower transport zone. The timing and magnitude of the landslide displacement are modulated by the intensity and duration of precipitation, as well as the antecedent water content of the landslide mass. In addition, we use a one-dimensional pore-water pressure diffusion model to estimate the rainfall-modulated pore-water pressure changes and hydraulic diffusivity. We find hydraulic diffusivity values between $6.8^{-2.0}_{+2.9}\times10^{-5}$ m^2/s, which agrees with ground-based measurements in this region. Displacement measurements on the hillslopes obtained from geodetic InSAR observations allow us to characterize the mobility, depth, and hydraulic diffusivity of slow-moving landslides.

1. Introduction

Landsliding is a mass wasting process driven by the force of gravity. Landslides generally occur on steep and mechanically weak slopes. Triggers include, but are not limited to, intense rainfall and snowmelt, disturbance of vegetative covers (e.g., wildfire and logging), disturbance of landforms (e.g., reservoir impoundment and road construction), and ground shaking (e.g., earthquakes and volcanic eruptions; e.g., Handwerger et al., 2013; Iverson, 2000; Kim et al., 2015; Liu et al., 2013; Mackey & Roering, 2011; Shi et al., 2017). Landslides affect many countries worldwide and often have catastrophic consequences (Petley, 2012). Monitoring landslide movements helps us better understand how the landslide mass propagates in space, how their motion evolves in time, and how external forcings, such as rainwater, control their behavior. Comprehensive landslide monitoring requires a widely applicable tool that can be used to measure the surface displacements even in remote landscapes. Over the past two decades, Interferometric synthetic aperture radar (InSAR) has been used to monitor landslides over large areas (e.g., Bovenga et al., 2006; Handwerger et al., 2019; Hilley et al., 2004; Massonnet & Feigl, 1998; Notti et al., 2014; Tofani et al., 2013; Wasowski & Bovenga, 2015). The InSAR-derived spatio-temporal displacements and the inferred landslide metrics can help facilitate hazard mitigation in population centers and transportation corridors.

The Shasta-Trinity and Six Rivers National Forest lands in northern California are vulnerable to landsliding due to steep slopes; disturbances such as wildfire, clearcut logging, and road construction (Mikulovsky et al., 2012); and a seasonally wet climate with about 90-cm annual rainfall. Our study area is located in near the border of Humboldt County and Trinity County (Figure 1a). In the middle to late 1950s, the vegetation cover
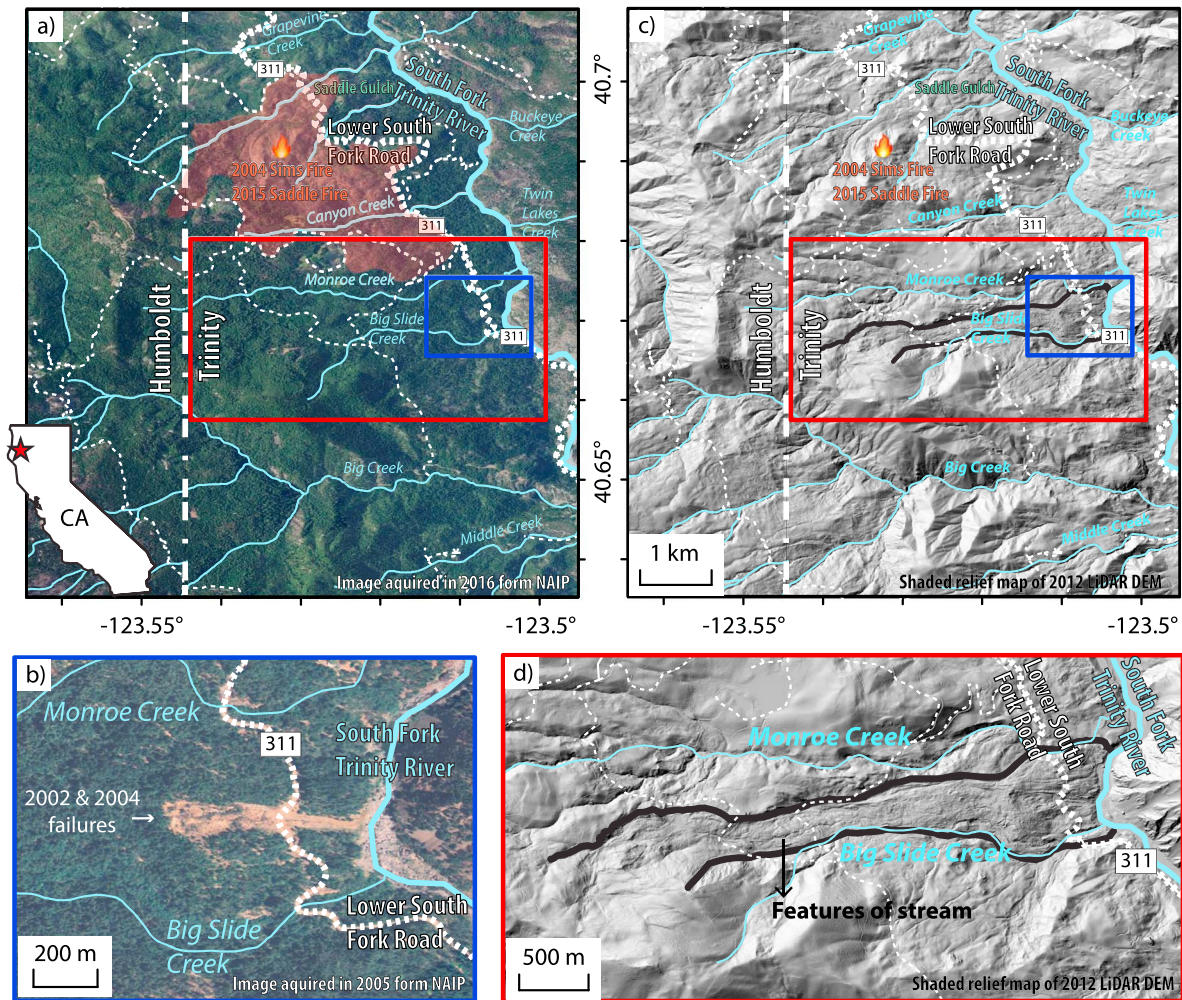
Figure 1. Landscape of the Monroe landslide complex. The blue lines show creeks and streams, and the thick blue lines show the South Fork Trinity River. The dotted white lines show roads, and the thick dotted white lines shows the Lower South Fork Road (a.k.a. Trinity County Road 311). (a) 2016 aerial photo of the landslide complex. The red star in the inset shows its location. The burns scars in red shade were exposed to both the 2004 Sims Fire and 2015 Saddle Fire. (b) 2005 aerial photo of the failure at the toe: the road was damaged and the deposits were transported to the South Fork Trinity River. (c) The shaded relief map from light detection and ranging (LiDAR) digital elevation model (DEM) of the landslide complex, and (d) the enlarged map of the target debris slide. The lateral margins of the active slide zone inferred from the geomorphic features are highlighted by thick black lines.

(mixed conifer and woodland, mainly tan oak and Douglas fir) in some inner gorge areas was removed for road construction. The vegetation clearance increased the groundwater recharge and degraded the slope stability (Fitzgerald, 2007). Most of the landslides in this area mobilize material of the Rattlesnake Creek Terrane, made up of mélange materials of Paleozoic marine sedimentary and metasedimentary rocks, and Mesozoic plutonic rocks (California Geological Survey, 2010). Detailed geologic units are described in Figure S1 in the supporting information. The landscape is characterized by a series of moderately steep landslide complexes and steep inner gorge landslides (slopes > 65%; U.S. Department of Agriculture Forest Service, 2015).

Here we investigate the Monroe landslide, which is a deep-seated (>5 m), rotational debris slide (e.g., Hungr et al., 2014). It is located upslope from Trinity County Road 311, near the Big Slide Campground, approximately 5 km northwest of Hyampom, California (Figure 1). The Monroe landslide was first mapped by U.S. Forest Service in 1986, and the area and volume were estimated to be 4 km^2 and 570 million m^3. However, the landslide volume was reevaluated in 2007 to be 52 million m^3 (Fitzgerald, 2007), 1 order of magnitude smaller than the previous estimate.

The Monroe landslide has been moving very slowly at a rate of ~2 cm/year for at least 70 years and has been continuously delivering sediments to the South Fork Trinity River (SFTR; Fitzgerald, 2007). The area is also

drained by many creeks flowing into the SFTR (Figure 1a). The landslide mass holds abundant underground and surface water, which causes the landslide to mobilize even on low topographic gradients (Fitzgerald, 2007).

Tension cracks at the landslide toe were detected in 2002. The slip plane at the toe occurred along a clay-rich serpentine gouge (Fitzgerald, 2007). Shortly after observations of the cracks were made, a small portion of the landslide failed and destroyed the Trinity County Road 311 in December after a series of rainstorms. Two years later, following the 2004 Sims Fire, a second small failure struck the same location. The 2002 failure had a volume of 6,500-m^3 debris, one fifth of which was delivered into the SFTR. The 2004 failure had a smaller volume but was accompanied by the enlargement of an active upslope head scarp (Fitzgerald, 2007). The areas north of the landslide lie within the footprints of both the Sims Fire (28 July to 5 August 2004, burned 16.3 km^2) and the Saddle Fire (10-29 June 2015, burned 5.4 km^2; Mondry, 2017), which likely contribute to increased sediment flux and landsliding (Figure 1). For the most severely burned watersheds, post-fire sediment delivery rates exceeded prefire background erosion rates by a factor of 3 to 5 (Mondry & Klingel, 2015). Potential slope failures may therefore create secondary hazards if the readily mobilized debris can temporarily dam the SFTR, and then cause flooding if the dam fails catastrophically.

The Monroe landslide complex was investigated as part of a road decommissioning project in 2007, with a focus on an improved understanding of the slide materials and geomorphological features (Fitzgerald, 2007). However, knowledge about the Monroe landslide is still fairly incomplete. The complicated landslide mobility is tied to heterogeneities of the soil materials, drainage from the incised streams, and disturbances from wildfires and road constructions. Here we use spaceborne L-band ALOS-1 PALSAR-1 and ALOS-2 PALSAR-2 data to retrieve the spatio-temporal displacements of the Monroe landslide, and we further explore its geometry, triggering mechanisms, and hydraulic properties (e.g., diffusivity).

2. Methodology

2.1. InSAR Data Analysis

Interferometric phase of repeat radar passes represents the difference in distance that the electromagnetic wave travels from the satellite to the ground target. Assuming that artifacts and noise are negligible, the differential phase is the summation of the topographic contributions associated with the spatial baseline (the distance between the satellite positions when imaging the same target) and the ground displacements (if any). InSAR processing benefits from a high-resolution and accurate digital elevation model (DEM) that is used to simulate the topographic contributions and get it removed from the interferograms, and also to geocode the images. We process the InSAR data using three sets of DEMs: 2000 SRTM DEM (30-m pixel spacing), 2012 light detection and ranging (LiDAR) DEM (1-m pixel spacing) and 2013 TanDEM-X DEM (12-m pixel spacing). Table S1 in the supporting information summarizes the geometric parameters and differences in geodetic datum of the DEMs. After an elevation calibration using a constant adjustment, we found elevation differences along the longitudinal extent of the landslide of up to 20 m (Figure S2). Assuming that the perpendicular baseline is 500 m, the phase change subject to 20-m DEM error is around 2 cm, corresponding to only one sixth of a full fringe cycle in ALOS L-band interferograms (Figure S3, see the supporting information for details). We applied the LiDAR DEM with the highest spatial resolution during InSAR data processing. The voids in the LiDAR DEM on the other side of the river east of the landslide were filled with the SRTM DEM.

Large displacement gradients exist where the slope changes in small-scale pixel clusters. Beyond that, the volume scattering of the forested landslide terranes may also contaminate the interferograms. Strong filtering of the interferograms may hide smaller-scale details of the phase changes and blur the landslide boundaries, while light filtering may be insufficient to cull out the noise. In the end, we adopted a filtering window with a small grid size of 20 m by 20 m to strike a balance between the resolution and accuracy before phase unwrapping.

The application of InSAR at this landslide is heavily limited by phase aliasing due to the large displacement gradient in the radar line-of-sight direction. To determine the displacement patterns, we first grouped the interferograms into different temporal intervals starting with the shortest time spans, that is, one orbital

cycle of 46 days. We traced the phase changes along the active slide zone from the head to the inner transport zone where larger displacements are apparent and identified five inflection points depicting sharp phase changes (black dots in Figure 2). Next, we analyzed the interferograms with two (92 days) and three orbital cycles (138 days). Sometimes, adjacent targets on and off the active slide body present similar phase values after a modulus of 2π shifts (e.g., 20070516-20071116 and 20090201-20090619 in Figure 2). To avoid phase unwrapping paths intersecting with the landslide boundaries and with displacement differences larger than 2π, we set up cutlines along the lateral boundaries (thick black lines in Figures 1 and 2). Manual correction (if needed) is introduced after phase unwrapping using SNAPHU where evident phase jumps still exist.

Unfortunately, due to issues with large spatial baselines, our dataset is not connected in time so we are not allowed to perform a time series inversion over the full time period. For example, the ALOS-1 PALSAR-1 satellite performed an orbital adjustment maneuver in the summer of 2008, 2.5 years after the launch of the satellite. The consequent interferometric baseline between images acquired before and after the orbital maneuver (e.g., the end of 2007, the beginning of 2008 to the end of 2008, and the beginning of 2009) is as large as several thousand meters (Figure S4). Although the baseline distances are reduced (<1,000 m) for some large-time-interval (≳2 years) pairs spanning the orbital maneuver, the interferograms are strongly degraded due to the temporal decorrelation and large displacements.

To estimate the average landslide velocity and time-series displacements, two sets of ALOS-1 interferograms (before and after the summer of 2008) are processed separately. The two ascending tracks of ALOS-1 data (P223 and P224) share a similar geometry, and the derived line-of-sight (LOS) velocities are nearly identical (Figure S5). To enhance the accuracy of the time-series analysis, we projected the estimates from these two tracks on to the downslope direction based on the topography (Hilley et al., 2004; Hu et al., 2016), and then integrated them using singular value decomposition. We also processed three descending tracks (P551, P555, and P556) of ALOS-1 data. But unfortunately, they do not show useful signals due to loss of coherence.

We also obtained ALOS-2 data from one ascending track (P68) and one descending track (P170) collected between 2015 and 2017. The data acquisitions of ALOS-2 are more limited: their time intervals are often more than half a year and thus not enough interferometric pairs are available for time series inversions. However, we can still estimate the LOS velocity by stacking four descending interferograms of P170 spanning different seasons. There is only one usable ALOS-2 interferogram in the ascending orbit (P68), and the displacement patterns are consistent with the ascending ALOS-1 data observed from a similar viewing geometry but with different time spans. We further integrated the ascending ALOS-1 and the descending ALOS-2 results to extract the quasi-3-D displacements by constraining the horizontal motions to hillslope aspects (Hu, Lu, Pierson, et al., 2018). The InSAR data used for the analysis and their geometric parameters are summarized in Table S2.

2.2. One-Dimensional Pore Pressure Diffusion Model

The infiltration of rainwater can elevate the pore-water pressure (use "pore pressure" hereafter) and reduce the Coulomb frictional strength of the landslide material. Therefore, precipitation modulates the timing and magnitude of landslide movements each year (e.g., Handwerger et al., 2013; Iverson & Major, 1987; Schulz, McKenna, et al., 2009; Terzaghi, 1943). Transient pore pressure changes can be characterized by a simple one-dimensional diffusion model (e.g., Cohen-Waeber et al., 2018; Handwerger et al., 2019; Iverson, 2000)

$$\frac{dP}{dt} = D\frac{d^2P}{dz^2} \quad t>0, z>0$$

where P is the transient pore pressure, t is time, D is the effective hydraulic diffusivity, and z is depth below the ground surface. This model describes the downward propagation of pore pressure waves and captures the first-order behavior of pore pressure changes. We model the pore pressures in order to better understand the interactions between rainfall and landslide velocity. More complex hydrologic models exist (e.g., Krzeminska et al., 2013; Leshchinsky et al., 2019), however, given the large uncertainties about subsurface landslide properties and our lack of ground-based data, we opt to use the simple 1-D model to interpret our InSAR results.
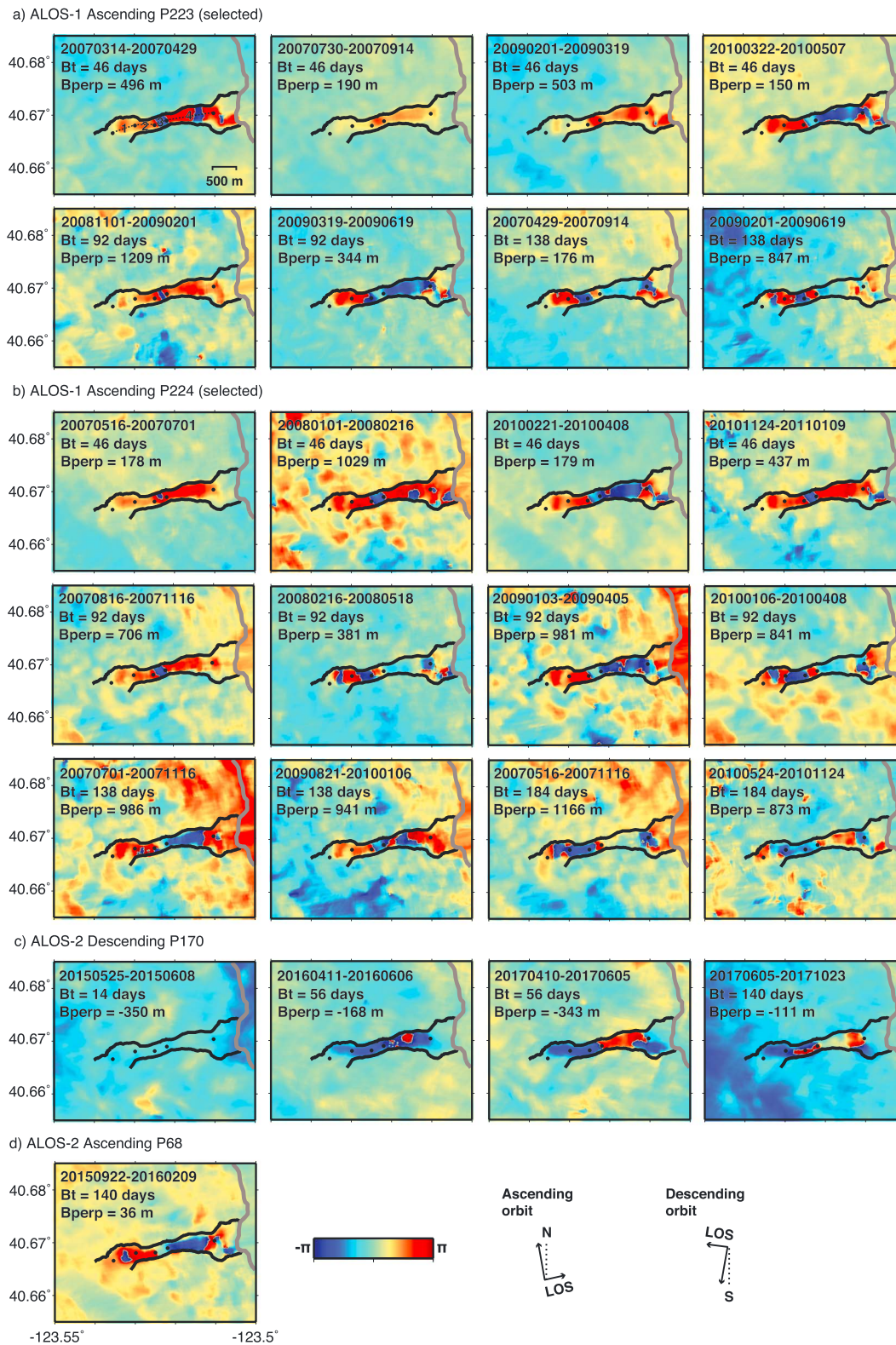
Figure 2. Wrapped interferograms of the study area. (a) Selected ALOS-1 P223 ascending results. (b) Selected ALOS-1 P224 ascending results. (c) ALOS-2 P170 descending results. (d) ALOS-2 P68 ascending result. The lateral margins are in thick black lines. Four kinematic elements dissected by sharp inflections (black dots) along the transport zone can be derived from the interferograms. The dashed line profile shown in the first image in panel a connects those inflections. The gray lines show the South Fork Trinity River.

The transient pore pressure near the surface

$$P = r \cdot R(t) \text{ at } z = 0$$

is in essence modulated by rainfall $R(t)$ on the surface ($z = 0$). An empirically calibrated infiltration scaling factor r scales the rainfall rate to a pressure value and characterizes hydraulic properties such as infiltration capacity and hydraulic conductivity. A solution to the diffusion equation under this surface boundary condition was given by (Carslaw & Jaeger, 1947; Handwerger et al., 2016)

$$P(z, t) = \frac{z}{2\sqrt{\pi D}} \int_0^t \frac{e^{-\frac{z^2}{4D(t-s)}}}{\sqrt{(t-s)^3}} P(s, z = 0) ds$$

In the Fourier domain, where $\mathscr{F}$ indicates the Fourier transform and $\mathscr{F}^{-1}$ indicates the inverse Fourier transform,

$$F(t) \sim \mathscr{F}\left[\frac{z}{2\sqrt{\pi D(t-s)^3}} e^{-\frac{z^2}{4D(t-s)}} \right]$$

$$G(s) \sim \mathscr{F}[P(t, z = 0)]$$

$$P(t, z) \sim \mathscr{F}^{-1}(F \cdot G)$$

These equations show that the timing, magnitude, and duration of pore pressure changes is strongly controlled by rainfall, the landslide thickness, and hydraulic diffusivity. Because we do not have ground-based measurements of pore pressure changes to calibrate our results, we normalized the modeled pore pressure changes and the landslide velocity, which allows us to explore their relative changes. Therefore, the effect of the infiltration scaling factor in the pore pressure model was eliminated. We then used the best fit cross correlation between the normalized pore pressure changes at depth and InSAR-derived surface velocity to constrain the effective hydraulic diffusivity of the landslide body. Given the same diffusivity, a thicker landslide allows for longer-wavelength pore pressure changes in time.

3. Results

3.1. Landslide Boundaries and Outlines of Kinematic Elements

The shaded relief map generated by the 1-m-posting 2012 LiDAR DEM reveals a hummocky landscape incised by multiple streams and roads. The elongated transport zone (stretching from inner gorge areas to the toe) can be easily identified with deep cutting features at the lateral margins, and a stream cutting through the longitudinal axis (Figure 1d). There is no clear geomorphic evidence, such as undercutting features, at the head and the toe that can be used to help identify their margins. Our InSAR observations show that the transport zone is moving continuously throughout the year and display the largest displacements (Figure 2). The landslide is moving slower in the head zone, and its margins are less clearly defined. Nevertheless, we can outline the active lobe of the head, which strikes about 210° to the southwest. The total active area is much larger than the surficial failures that occurred at the toe in 2002 and 2004. These failures displaced soil, rock, and vegetation, which together with the road cuts in the transverse direction, seem to complicate the toe environment, where we see unusual patterns in some interferograms (e.g., 20080216-20080518, 20090103-20090405, 20090319-20090619, 20100221-20100408, 20100322-20100507, and 20150922-20160209 in Figure 2), suggesting subsurface disconformities.

The variable displacement patterns (i.e. nonuniform motions) displayed by the landslide are a result of the interplay of complex factors, such as local geometry (slope, thickness, and width), rheological variations, incised streams and roads, and the potential changes in frictional strength along the lateral and basal sliding surfaces. We believe that the large phase gradients in the interferograms represent the boundaries between kinematic elements. Based on this concept, we divide the transport zone into four distinct kinematic elements. Element 3 in the longitudinal center shows a phase change peak where the displacement is the
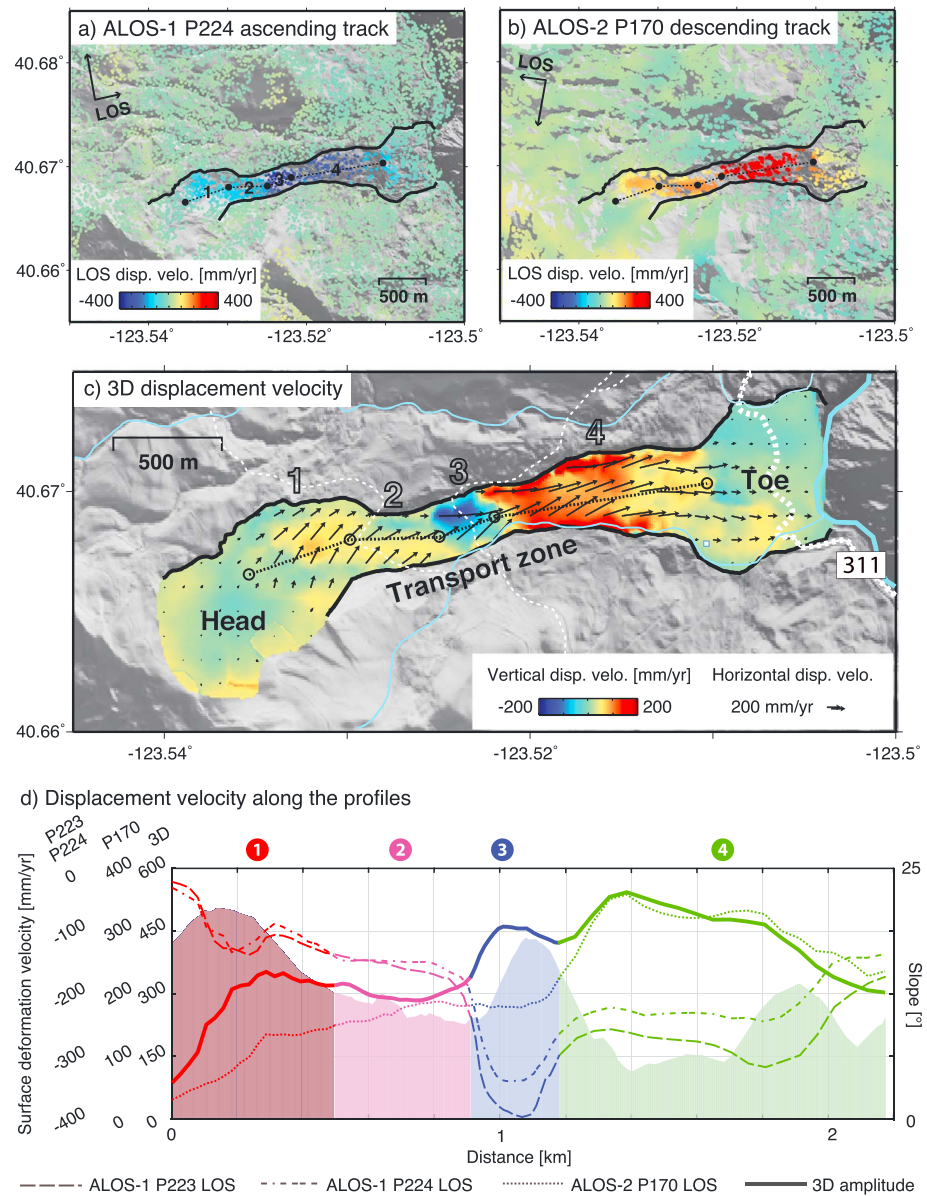
Figure 3. Landslide velocity of the Monroe landslide. Radar line-of-sight (LOS) velocity of (a) ALOS-1 P224 ascending data and (b) ALOS-2 P170 descending data. ALOS-1 P223 results are similar to P224 due to a similar imaging geometry and are shown in Figure S5. In panels a and b, positive values suggest that the target moves toward the satellite. The dotted lines show the longitudinal profiles across four kinematic elements with the inflection points marked by black dots/circles. (c) 3-D velocity field. The color in panel c shows inferred vertical displacements where positive values mean uplift. The arrows show the estimated horizontal displacement rates assuming downslope transport, with the direction and magnitude indicated. The cyan lines are the South Fork Trinity River (SFTR) and its tributaries. The white dotted lines are roads and trails. (d) Displacement rates (in mm/year, referring to the left Y axis) along the profiles in the transport zone plotted against the local slope (in degrees, referring to the right Y axis) in the shaded background. P223, P224, and P170 indicate the LOS measurements of the corresponding tracks. The 3-D amplitude is the amplitude of 3-D displacement vector, that is, $\sqrt{E^2 + N^2 + U^2}$.

largest. The amount of phase change decreases between elements 2 and 3 is larger than that between 3 and 4, indicating a smaller amount of deformation uphill than downhill.

3.2. Velocities of the Complex Kinematic Elements

The largest LOS velocities (>350 mm/year) occur near the longitudinal center (element 3) where there is a slightly oversteepened (>15°) facet (Figures 3a and 3b). Hillslopes adjusted to the oversteepening by mass

wasting processes, that is, quickly transporting the sediments and reducing the slope angles downslope (element 4 in Figure 3d; Stimely, 2009). The head and toe have larger slope angles, yet the velocities are smaller than those in the middle transport zone. This might be due to the wider landslide body at the head and toe. Overall, there is no evident correlation between the landslide velocity and the slope angles for this landslide.

The 2007-2011 ascending-orbit LOS velocity is similar to that of the 2015-2017 descending LOS velocity, but the sign is opposite because the dominantly horizontal displacements are in directions away from and toward the sensors, respectively (Figure 3). The 3-D velocity map shows that the largest subsidence is observed at element 3, where the slope angle increases, and the transport zone narrows. Surface uplift is mainly observed at the downslope kinematic element 4. The sharp steps in both vertical and horizontal components are considered to be intralandslide normal and thrust faults as they are consistent with these deformation features. Assuming that the landslide faults dip downhill, normal faults transect perpendicular to the downslope direction at the upslope section of element 3 where the slope steepens, while thrust faults transect at the downslope section of element 3 where the landslide surface begins to flatten. Some trails cross and streams incise the area and may also affect the water drainage and modulate the slide motion. The topography-inferred horizontal vectors change from the north-to-northeast at the head to the east at the toe. The largest horizontal motions are located at elements 3 and 4. The complicated displacement patterns at the toe in the interferograms partially overlap with the road-damaging failures from 2002 and 2004. The derived velocity fields further suggest that the south part at the toe moves upward and eastward, while the north part remains nearly stationary during the observation period. This contrast suggests subsurface disconformities and/or temporal variability.

3.3. Landslide Movements and Rainfall-Modulated Pore Pressure

To better understand the underlying forces driving landslide motion, we investigate the correlation between landslide displacement, rainfall, and modeled pore pressure. The nearest rainfall monitoring gauge is ~20.6 km east of the Monroe landslide, and the data were obtained from the Department of Water Resources, California Data Exchange Center. We first derived the linearly detrended/seasonal downslope displacement at each kinematic element during 2007-2011 (Figure 4b). The elements with larger movements, and thus higher signal-to-noise ratio, depict more pronounced seasonal variations (Hu, Lu, & Wang, 2018). The LOS velocity is then calculated from the first derivative of the interpolated cumulative displacement time series using three independent sinusoidal functions. The average seasonal displacement time series and displacement rates are both cyclic with a period of about 1 year. Generally, the maximum rates occur in March and minimum rates in September (Figure 4c). This is more obvious in the condensed results of one calendar year (Figure 6, further discussed in section 4.3). The precipitation also varies seasonally, with the rainy season lasting from about November through April and very little rain during the intervening summer months.

3.4. Depth of Landslide Basal Surface

The geomorphic features of the failed toe of the Monroe landslide suggest at least 10-m depth (Fitzgerald, 2007). However, there have been no other estimates of the depth to the basal surface for the other parts of the landslide. We first consider estimates of landslide thickness based on empirically derived scaling of the depth D and area A of deep-seated landslides: $D = \alpha A^{\gamma}$ (Dussauge et al., 2003; Fuyii, 1969; Simonett, 1967), where the indices α and γ are generally in ranges of 0.066-0.08 and 0.42-0.44, respectively (Handwerger et al., 2013; Larsen et al., 2010; Simoni et al., 2013). The active area of the Monroe landslide is about 1 km^2, so the depth is estimated to be 21 to 35 m. We use these values as bounds in the mass conservation model and the pore pressure diffusion model (see section 4.3).

Four kinematic elements with distinct velocities along the transport zone suggest that there are variations in the landslide thickness. Based on the conservation of mass, we invert for the landslide depth and thus the basal geometry using 3-D surface displacements. The fundamental theorem is that the horizontal mass flux divergence is balanced by the rate of thickness changes (Booth et al., 2013; Delbridge et al., 2016; Hu, Lu, Pierson, et al., 2018). We set the maximum landslide depth as 35 m according to the empirical relationship between landslide area and depth. We assume landslide deformation across the entire depth range by Newtonian viscous flow and that the debris materials share a constant rheology (Hu, Lu, Pierson, et al., 2018).
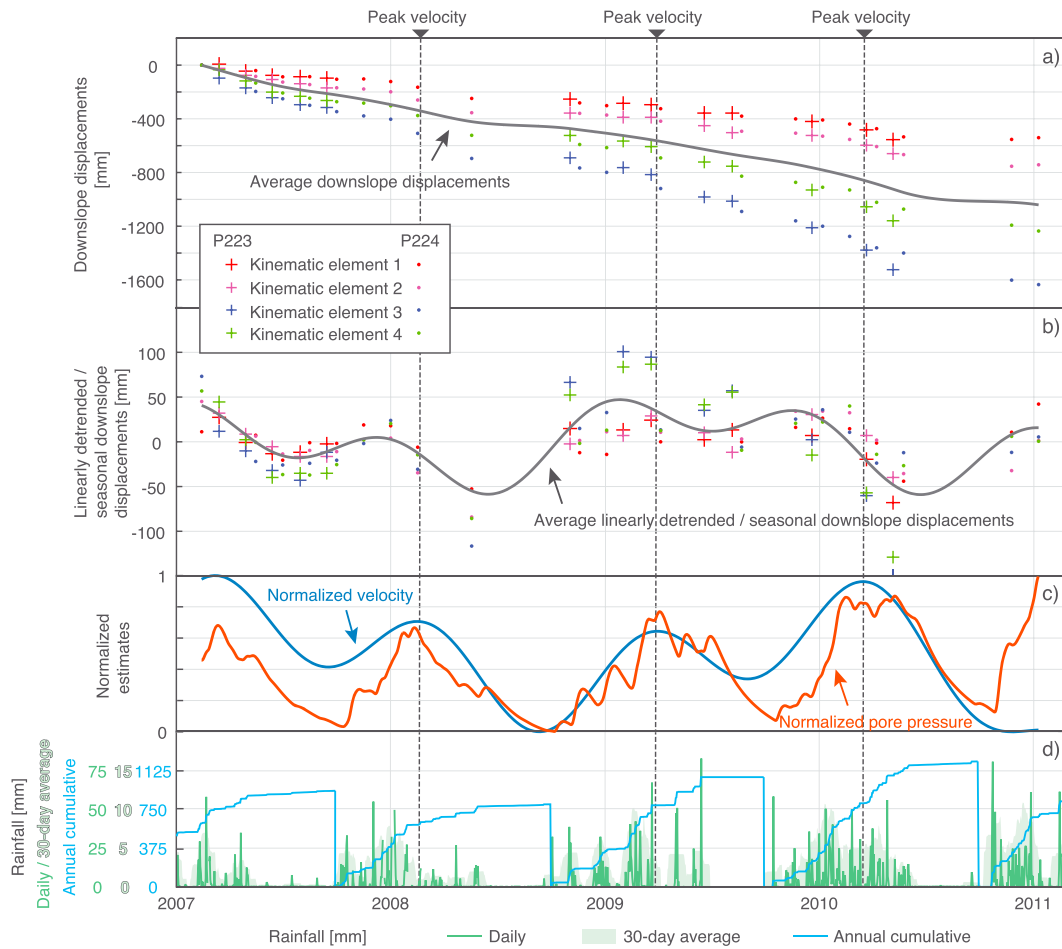
Figure 4. (a–d) Landslide displacements, precipitation, and the modeled pore pressure. ALOS-1 line-of-sight (LOS) displacements have been projected into the downslope direction. Crosses show the downslope displacement derived from P223 data, and dots show the downslope slip derived from P224 data. The symbol colors represent the estimates of the indicated kinematic elements. The thick gray line (a) shows the interpolated average cumulative downslope displacement of the transport zone. The thick gray line in (b) shows the interpolated average linearly-detrended/seasonal downslope motion. (c) The interpolated normalized velocity together with the normalized pore pressure based on the one-dimensional diffusion model from 2007 to 2011. The occurrences of peak velocity of each water year are indicated with the vertical dashed line. (d) The green lines show the daily precipitation, and the blue lines show the cumulative precipitation data (reset to zero on 1 October).

The solution (Figure 5) suggests a pronounced thickening near the transition zone from subsidence to uplift between elements 3 and 4 (referred to as the key transition hereafter). Upslope of the key transition, elements 1 and 2 remain stable or experience subtle uplift, and the derived basal surface depth does not vary much. Landslide thickness declines slightly where the landslide enters the narrow part of element 3 where the slope steepens and the surface subsides, and then the thickness increases in order to compensate for the inflow of mass until the key transition. Downslope of the key transition the landslide at element 4 becomes thinner to maintain mass conservation. The basal surfaces are very likely irregular around the toe area considering the displacement variations we observed, probably affected by the previous runout failures cutting through the toe area and the road constructions.

The landslide depth inversion relies on the 3-D surface velocities, which involve ambiguities from the incomplete solution using the ascending and descending InSAR measurements spanning different years, the topography-inferred horizontal vectors, and also from the spatial interpolation that inevitably produces some outliers at the boundaries. Varying properties among the kinematic elements, such as in the rheology of the landslide material and/or the basal shear zone, and the intervening structural discontinuities further contribute to the uncertainty. Additionally, we lack *prior* known constraints such as some basal depth
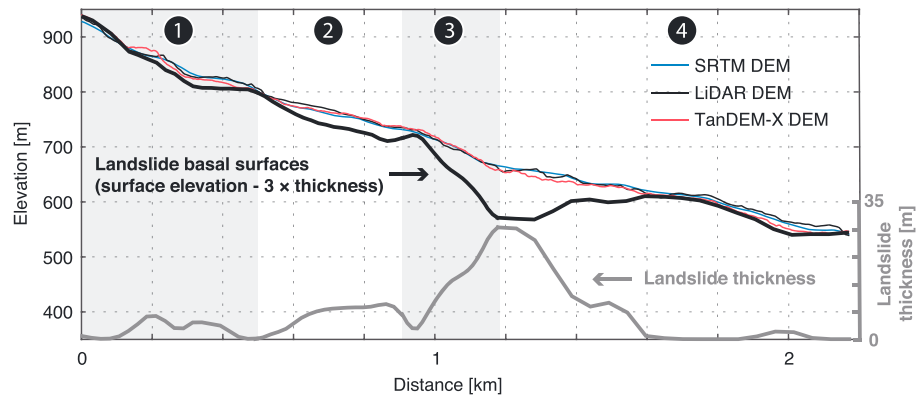
Figure 5. Ground surface and basal surface elevation along the kinematic elements of the landslide transport zone (dotted-line profiles in Figure 3). The thin lines show the elevation of different digital elevation models (DEMs), and the postings of DEMs have been unified and resampled to 12 m. The thick black line shows the exaggerated basal sliding surface. The thick gray line shows the landslide thickness.

measurements from boreholes. Nevertheless, given the lack of field constraints, we can provide provisional depth estimates using only the remotely sensed displacement measurements.

4. Discussion

4.1. Implications of Surface Uplift at the Downslope Above the Toe

The changes in landslide geometry may impart important mechanical controls on the landslide motion. Surface uplift has been mainly observed in the lower part of the transport zone (i.e., kinematic element 4 in Figure 3), where the widening and perhaps deepening slide zone may be sufficient to accommodate the mass, and thus, the accumulation at the toe is less evident. Field estimates at the toe suggest that the grain size of half of the landslide material is greater than 2 mm, whereas 90% of the shear plane material consists of fine-grained clay-rich serpentine (Fitzgerald, 2007). Thus, the porosity of the landslide materials may span a wide range and vary in space. The ground uplift at element 4 could be primarily due to the mass accumulation (see section 3.4) considering the high rate (20 cm/year), and partly, could be a result of the shear-induced dilation if the porosity is below the critical value (Iverson et al., 2015). The wildfire that occurred immediately north of the Monroe landslide may have even helped to promote dilation by reducing the porosity because of (1) the structural alteration from the collapse of aggregates and the loss of macropores, (2) the clogging of voids by the ash and the dispersed clay minerals when wetting, and (3) the loss of soil invertebrates (Certini, 2005). Assuming an unchanged critical-state porosity after the fire, the ensuing soil dilation could be larger than usual. Accompanying the soil dilation, a reduction of pore pressure will stabilize the system through the enhanced effective stress and shear resistance (e.g., Iverson et al., 2015; Schulz, McKenna, et al., 2009). While this stabilizing mechanism may be important, it is possible that eventually the increased porosity may become larger than during steady-state conditions, and contraction, increased pore pressure, and decreased strength may occur upon shearing. Additionally, the consolidation of fine-grained materials also reduces the air and water in the pore space. Episodic dilation and contraction usually take turns during the shear-induced strengthening and weakening processes. The long-term uplift at element 4 seems to hint at but is not direct evidence for an overall strengthening. However, runaway instability can occur when sufficient pore pressures develop along the slip surface after extreme rainfall or from shear-induced contraction (e.g., Handwerger et al., 2019; Iverson et al., 2015). In situ continuous displacement, porosity, and pore pressure measurements are required to quantify these mechanical-hydrologic controls.

4.2. Correlation of Seasonal Precipitation and Landslide Motion

The intensity, duration, and frequency of the rainfall, as well as the rainfall condition in the previous year(s), can affect the timing and magnitude of landslide movements. The modest seasonal displacements during 2008-2009 seem to stand out in the time series, and there could be two plausible explanations. Recall that the interferograms are not fully connected due to the orbital maneuver in the summer of 2008. Although
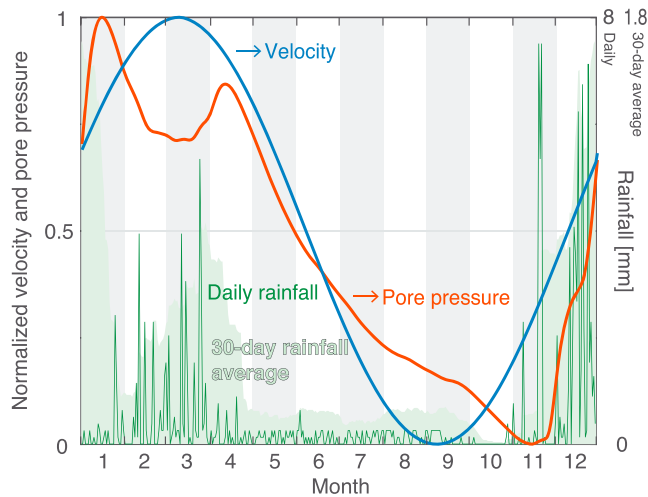
Figure 6. The normalized velocity against the normalized pore pressure over one calendar year, superimposed on the average daily rainfall.

we integrate results of P223 and P224 through singular value decomposition to enhance the data sampling, the results in 2008 could still be impacted by the limited number of acquisitions and poorer quality of interferograms due to decorrelation. In addition, the precipitation from 2008 to 2009 was somewhat unusual. Water year 2008 (1 October 2007 to 30 September 2008) was a relatively dry year with low peaks and low totals, presumably establishing a low water content in the soil matrix. Subsequently, the period from late 2008 to early 2009 witnessed several short-term storms with high intensity, which are represented by steps in the cumulative precipitation (Figure 4d). Concomitant with the precipitation records, the modeled pore pressure shows a lower transient in late 2008 (Figure 4c). The downslope displacement from 2008 to 2009 is smaller than that of the other years. After linear trend removal of the cumulative displacements, the remainder shows a large rise in displacement in late 2008 and a slight decline in early 2009 (Figure 4b). In general, the seasonal movement in 2009 is small, although the rainfall total is above average. This suggests that the landslide motion is sensitive to both the rainfall intensity and duration. Short-term rain storms may not be able to mobilize the landslide, as the rainwater can be immediately drained by overland flow or via shallow groundwater paths. Consequently, the pore pressure may not increase to the critical state that drives accelerated slip. However, transient acceleration after rain storms is possible. For instance, the Slumgullion landslide, Colorado, accelerates within hours after a rainstorm when the increased pore pressures could only propagate to the shallow parts of the marginal faults (Schulz et al., 2017). Due to the relatively coarse time resolution of our dataset, we cannot resolve any potential short-term accelerations that follow individual storms. Future studies with L-band data collection spanning more years and at a higher sampling rate, as will be possible with the ground-based InSAR systems and/or the NASA-ISRO SAR (NISAR) mission currently planned to be launched in 2021, can help us better understand the direct role of precipitation in the progressive landslide movements.

4.3. Landslide Hydraulic Diffusivity

Based on the simple one-dimensional pore pressure diffusion equation, the effective hydraulic diffusivity can be constrained by the temporal cross correlation between the normalized landslide velocity and transient pore pressure at a given depth. Deep seated, slow-moving landslides occurring in clay-rich material typically have hydraulic diffusivity less than 10^{-4} m^2/s (Iverson & Major, 1987; Schulz, Kean, & Wang, 2009). For example, the field measurement of effective hydraulic diffusivity is 10^{-6} m^2/s at the Minor Creek landslide, northern California (Iverson, 2000; Iverson & Major, 1987), and 7.8×10^{-5} m^2/s on Slumgullion landslide (Schulz, Kean, & Wang, 2009). These values are within the range of values estimated by previous studies that have used diffusion models in California. Estimated diffusivity at Blakemont landslide in the San Francisco East Bay Hills is 1.5×10^{-6} m^2/s (Cohen-Waeber et al., 2018) and is 1.18×10^{-5} m^2/s at Mud Creek landslide, California (Handwerger et al., 2019). Therefore, we set the search windows for the characteristic diffusivity to be 10^{-6} to 10^{-4} m^2/s. There is a tradeoff between diffusivity and landslide depth in the pore pressure diffusion models. Since we do not have field-based measurements of landslide thickness, we explore a range values between 21 to 35 m (section 3.4).

To further constrain the characteristic diffusivity for the landslide mass, we consider two scenarios: (a) from 2007 to 2011 spanning the SAR acquisition dates and (b) one averaged calendar year. For the 2007 to 2011 results, the displacement measurements preserve the yearly variations due to a limited temporal sampling of SAR data, but the pore pressures can be characterized in more details benefiting from the daily rainfall records (Figure 4c). For the analysis condensed to one calendar year, we use the median daily rainfall over a 10-year period from 2007 to 2016 (Figure 6). The rainfall records in 2006 are incomplete so we do not consider the water year 2006. We allow the characteristic landslide thickness to deviate 5% from the best fit value, and we consider solutions within 0.2% of the minimum residual, the characteristic diffusivity is constrained to be $5.63^{-0.79}_{+0.9} \times 10^{-5}$ m^2/s for the one year period, and $7.94^{-1.44}_{+1.79} \times 10^{-5}$ m^2/s for the period between 2007 and 2011, respectively (Figure S6).

Estimates of the pore pressure from rainfall data remain uncertain. Given the tradeoffs between the landslide depth and diffusivity, high-correlation, and small-residual solutions span a wide range (Figure S6). In addition, this method is based on two general and overly simplified assumptions: (1) the landslide velocity measured at the ground surface responds directly to pore pressure changes deep within the landslide body and (2) a single 1-D diffusivity characterizes the hydraulic properties of complex 3-D landslide (Handwerger et al., 2019; Schulz, Kean, & Wang, 2009). However, these fundamental assumptions are not always supported by observations. Contrasting relations have been observed in the strike-slip sliding surfaces along the lateral margins of the Slumgullion landslide (e.g., Schulz et al., 2017; Schulz, Kean, & Wang, 2009) and the Two Towers landslide in Northern California (Schulz et al., 2018). For example, Schulz et al. (2018) argue that during the wet season, the swelling of clay-rich soil enhances the resistance at the lateral margins, which can counter the weakening at the base due to elevated pore pressure. Much remains to be learned about the interactions between landslide movements and pore pressure changes. Future work should include a detailed analysis of the horizontal and vertical pore pressure diffusion processes and the feedbacks from the bounding surfaces.

4.4. Comparisons between the Monroe landslide, CA, and Slumgullion landslide, CO

The spatial variations of displacements over the Monroe landslide resemble that of the well-studied Slumgullion landslide (e.g., Delbridge et al., 2016; Guzzi & Parise, 1992; Schulz et al., 2017; Schulz, Kean, & Wang, 2009; Schulz, McKenna, et al., 2009). The Monroe landslide has an average surface slope of 12°, 3.2-km length, 250-m width, and 1 km^2 in area; Slumgullion has an average 8° surface slope, 3.9-km length, 300-m width, and 1.5 km^2 in area (Guzzi & Parise, 1992; Schulz et al., 2017). They both are debris slides, highlighted by distinct and persistent kinematic elements, and controlled by strike-slip faults along the lateral margins, normal/thrust faults transecting at width, and basal surfaces (Guzzi & Parise, 1992). Both landslides have the most rapid movements near their longitudinal center and the slowest motions at the head and toe, and both are nested within a larger and dormant landslide complex.

They are also different in some aspects. The Monroe landslide is classified as a rotational debris slide (Fitzgerald, 2007), but Slumgullion is a translational debris slide (Schulz et al., 2017; Schulz, Kean, & Wang, 2009). Another distinct difference is the rate of motion: the Monroe landslide is moving at up to ~0.65 m/year, while Slumgullion has moved persistently for ~300 years at a speed one order larger (~7 m/year). The vegetation is much denser on the Monroe landslide and thus more vulnerable to decorrelation during InSAR data processing.

During the cyclic seasons, Slumgullion moves slowest during winter-spring and moves fastest during spring-summer (Coe et al., 2003; Schulz et al., 2017; Schulz, Kean, & Wang, 2009; Schulz, McKenna, et al., 2009). The Monroe landslide moves slowest in fall (September) and moves fastest in spring (March; Figure 6). The disparity in the timing of peak velocity directly relates to the timing and form of precipitation that drives the landslide motion (Gong et al., 2019). In southwestern Colorado, precipitation occurs throughout the year, falling mainly as snow in winter-spring, and as rain at other times. Therefore, the pore pressure is actually low during winter-spring. Afterward, the warming temperatures during spring-summer let abundant snowmelt infiltrate the subsurface. On the other hand, in northern California the precipitation mainly falls as rain in winter-spring. These differences in the spatio-temporal landslide behavior highlight the importance of climate on controlling landslide motion.

Another implication to the Monroe landslide can be drawn from the transient speed up within hours after the rainfall in Slumgullion (Schulz et al., 2017). Narrow slides usually have a large portion of the unstable materials directly in contact with the lateral surfaces extending from the ground surface. During the rainy season, pore pressure reaches the sides and the base at different time and amount. The time-varying effective stress and frictional resistances from the sides and the base may counter or enhance an overall resistance. The lateral fault surfaces and the basal surfaces, together, regulate the landslide movements (e.g., Gomberg et al., 2011; Schulz et al., 2017).

4.5. Safety Concerns

Other less deforming but unstable catchments are identified in patchy distributions over this watershed. Of particular notice is the hillslope affected by 2004 and 2015 wildfires, which are subject to accelerated soil erosion, and have high potentials to deliver the sediments to the fluvial systems (U.S. Department of Agriculture

Forest Service, 2015). More recently, the Sims Riparian Enhancement project was proposed for the 108 acres in the Big Slide Creek- SFTR watersheds, involving rehabilitation and reforestation (Mondry, 2017). This project will be entirely manually implemented, including hand cutting, hand piling and burning, planting, and release (Mondry & Klingel, 2015). A large workforce will be deployed in the large unstable terranes. Field operations and the use of the County Road need to be restricted during and after stormy days. Activation of the landslides in this area should be monitored in real time to ensure safety.

4.6. Feasibility of Other SAR Data Sets

C-band spaceborne SAR data such as ENVISAT and Sentinel-1 data sets, as tested, are not suitable for landslide monitoring at this location due to the trade-off between the coherence and spatial resolution. The coherence is not ideal in the vegetated terrain with large displacement, so that typical multilooks (e.g., 20 to 4 for ENVISAT data and 6 to 23 for Sentinel-1 data) are needed to enhance the coherence. The original resolutions in azimuth and slant range directions for ENVISAT data are about 6 and 9 m, respectively, and those for Sentinel-1 data are about 23 and 3 m, respectively. The use of multilooks further degrades the spatial resolution, and therefore, the landslide motion of narrow width (~200 m) is nearly unresolvable. Long-wavelength airborne SAR missions, such as the L-band and S-band Uninhabited Aerial Vehicle Synthetic Aperture Radar (UAVSAR), provide multiple options for the acquisition time intervals and viewing geometries, and images the ground at high spatial resolution as well, so they are the preferred imaging systems if deployed in this area.

5. Conclusions

Landslide metrics, including spatio-temporal displacements, boundaries, thickness, and hydraulic diffusivity, have been retrieved for an ~1-km^2 debris slide using L-band ALOS data sets, precipitation data, and DEMs. The landslide displays persistent seasonal downslope motion during 2007-2011 and 2015-2017. Normal and thrust faults that transect the landslide segregate the transport zone into four major kinematic elements. The landslide displays its largest displacements in the central kinematic element where it narrows and steepens. The estimated landslide thickness reaches a maximum at the transition between compression and extension near the exit of the central kinematic element. Uplift is mainly observed in the lower transport zone. Previously, failure at the toe seems to affect the landslide behavior, where the movements are mainly observed to its south, while the north part is mostly stable. The Monroe landslide movements fluctuate seasonally—moving fastest in March and slowest in September. Additionally, the correlation between rainfall-modulated modeled pore pressure and InSAR-derived landslide speed suggests a characteristic diffusivity of $6.8^{-2.0}_{+2.9} \times 10^{-5}$ m^2/s, which is in the range of the estimates for other landslides in northern California.

References

Booth, A. M., Lamb, M. P., Avouac, J.-P., & Delacourt, C. (2013). Landslide velocity, thickness, and rheology from remote sensing: La Clapière landslide, France. *Geophysical Research Letters*, *40*, 4299–4304. https://doi.org/10.1002/grl.50828

Bovenga, F., Nutricato, R., Refice, A., & Wasowski, J. (2006). Application of multi-temporal differential interferometry to slope instability detection in urban/peri-urban areas. *Engineering Geology*, *88*(3–4), 218–239. https://doi.org/10.1016/j.enggeo.2006.09.015

California Geological Survey (2010). Geologic map of California, California Department of Conservation.

Carslaw, H. S., & Jaeger, J. C. (1947). *Conduction of heat in solids*, (1st ed.pp. 43–45). Oxford: Oxford at the Clarendon Press.

Certini, G. (2005). Effects of fire on properties of forest soils: A review. *Oecologia*, *143*(1), 1–10. https://doi.org/10.1007/s00442-004-1788-8

Coe, J. A., Ellis, W. L., Godt, J. W., Savage, W. Z., Savage, J. E., Michael, J. A., et al. (2003). Seasonal movement of the Slumgullion landslide determined from Global Positioning System surveys and field instrumentation, July 1998–March 2002. *Engineering Geology*, *68*(1-2), 67–101. https://doi.org/10.1016/S0013-7952(02)00199-0

Cohen-Waeber, J., Bürgmann, R., Chaussard, E., Giannico, C., & Ferretti, A. (2018). Spatiotemporal patterns of precipitation-modulated landslide deformation from independent component analysis of InSAR time series. *Geophysical Research Letters*, *45*, 1878–1887. https://doi.org/10.1002/2017GL075950

Delbridge, B. G., Bürgmann, R., Fielding, E., Hensley, S., & Schulz, W. H. (2016). Three-dimensional surface deformation derived from airborne interferometric UAVSAR: Application to the Slumgullion Landslide. *Journal of Geophysical Research: Solid Earth*, *121*, 3951–3977. https://doi.org/10.1002/2015JB012559

Dussauge, C., Grasso, J.-R., & Helmstetter, A. (2003). Statistical analysis of rockfall volume distributions: Implications for rockfall dynamics. *Journal of Geophysical Research*, *108*(B6), 2286. https://doi.org/10.1029/2001JB000650

Fitzgerald, J. (2007). Monroe slide mass failure report, prepared for: Trinity County Resource Conservation District. Graham Matthews and Associates.

Fuyii, Y. (1969). Frequency distribution of landslides caused by heavy rain-fall. *Journal of the Seismological Society of Japan*, *22*(3), 244–247. https://doi.org/10.4294/zisin1948.22.3_244

Gomberg, J., Schulz, W., Bodin, P., & Kean, J. (2011). Seismic and geodetic signatures of fault slip at the Slumgullion Landslide Natural Laboratory. *Journal of Geophysical Research*, *116*, B09404. https://doi.org/10.1029/2011JB008304

Gong, W., Darrow, M. M., Meyer, F. J., & Daanen, R. P. (2019). Reconstructing movement history of frozen debris lobes in northern Alaska using satellite radar interferometry. *Remote Sensing of Environment*, *221*, 722–740. https://doi.org/10.1016/j.rse.2018.12.014

Guzzi, R., & Parise, M. (1992). Surface features and kinematics of the Slumgullion landslide, near Lake City, Colorado, in U. S. Geological Survey Open-file Report 92-252 (Reston, VA).

Handwerger, A. L., Huang, M.-H., Fielding, E. J., Booth, A. M., & Bürgmann, R. (2019). A shift from drought to extreme rainfall drives a stable landslide to catastrophic failure. *Scientific Reports*, *9*(1), 1569. https://doi.org/10.1038/s41598-018-38300-0

Handwerger, A. L., Rempel, A. W., Skarbek, R. M., Roering, J. J., & Hilley, G. E. (2016). Rate-weakening friction characterizes both slow sliding and catastrophic failure of landslide. *Proceedings of the National Academy of Sciences of the USA*, *113*(37), 10,281–10,286. https://doi.org/10.1073/pnas.1607009113

Handwerger, A. L., Roering, J. J., & Schmidt, D. A. (2013). Controls on the seasonal deformation of slow-moving landslides. *Earth and Planetary Science Letters*, *377-378*, 239–247. https://doi.org/10.1016/j.epsl.2013.06.047

Hilley, G. E., Bürgmann, R., Ferretti, A., Novali, F., & Rocca, F. (2004). Dynamics of slow-moving landslides from permanent scatterer analysis. *Science*, *304*(5679), 1952–1955. https://doi.org/10.1126/science.1098821

Hu, X., Lu, Z., Pierson, T. C., Kramer, R., & George, D. L. (2018). Combining InSAR and GPS to determine transient movement and thickness of a seasonally active low-gradient translational landslide. *Geophysical Research Letters*, *45*, 1453–1462. https://doi.org/10.1002/2017GL076623

Hu, X., Lu, Z., & Wang, T. (2018). Characterization of hydrogeological properties in Salt Lake Valley, Utah Using InSAR. *Journal of Geophysical Research: Earth Surface*, *123*, 1257–1271. https://doi.org/10.1029/2017JF004497

Hu, X., Wang, T., Pierson, T. C., Lu, Z., Kim, J., & Cecere, T. H. (2016). Detecting seasonal landslide movement within the Cascade landslide complex (Washington) using time-series SAR imagery. *Remote Sensing of Environment*, *187*, 49–61. https://doi.org/10.1016/j.rse.2016.10.006

Hungr, O., Leroueil, S., & Picarelli, L. (2014). The Varnes classification of landslides, an update. *Landslides*, *11*(2), 167–194. https://doi.org/10.1007/s10346-013-0436-y

Iverson, R. M. (2000). Landslide triggering by rain infiltration. *Water Resources Research*, *36*(7), 1897–1910. https://doi.org/10.1029/2000WR900090

Iverson, R. M., George, D. L., Allstadt, K., Reid, M. E., Collins, B. D., Vallance, J. W., et al. (2015). Landslide mobility and hazards: Implications of the 2014 Oso disaster. *Earth and Planetary Science Letters*, *412*, 197–208. https://doi.org/10.1016/j.epsl.2014.12.020

Iverson, R. M., & Major, J. J. (1987). Rainfall, groundwater flow, and seasonal movement at Minor Creek landslide, northwestern California: Physical interpretation of empirical relations. *Geological Society of America Bulletin*, *99*(4), 579–594. https://doi.org/10.1130/0016-7606(1987)99<579:RGFASM>2.0.CO;2

Kim, J. W., Lu, Z., Qu, F., & Hu, X. (2015). Pre-2014 mudslides at Oso revealed by InSAR and multi-source DEM analysis. *Geomatics, Natural Hazards and Risk*, *6*(3), 184–194. https://doi.org/10.1080/19475705.2015.1016556

Krzeminska, D. M., Bogaard, T. A., Malet, J.-P., & van Beek, L. P. H. (2013). A model of hydrological and mechanical feedbacks of preferential fissure flow in a slow-moving landslide. *Hydrology and Earth System Sciences*, *17*(3), 947–959. https://doi.org/10.5194/hess-17-947-2013

Larsen, I. J., Montgomery, D. R., & Korup, O. (2010). Landslide erosion controlled by hillslope material. *Nature Geoscience*, *3*(4), 247–251. https://doi.org/10.1038/ngeo776

Leshchinsky, B., Olsen, M. J., Mohney, C., O'Banion, M., Bunn, M., Allan, J., & McClung, R. (2019). Quantifying the sensitivity of progressive landslide movements to failure geometry, undercutting processes and hydrological changes. *Journal of Geophysical Research: Earth Surface*, *124*, 616–638. https://doi.org/10.1029/2018JF004833

Liu, P., Li, Z., Hoey, T., Kincal, C., Zhang, J., Zeng, Q., & Muller, J.-P. (2013). Using advanced InSAR time series techniques to monitor landslide movements in Badong of the Three Gorges region, China. *International Journal of Applied Earth Observation and Geoinformation*, *21*, 253–264. https://doi.org/10.1016/j.jag.2011.10.010

Mackey, B. H., & Roering, J. J. (2011). Sediment yield, spatial characteristics, and the long term evolution of active earthflows determined from airborne LiDAR and historical aerial photographs, Eel River, California. *Geological Society of America Bulletin*, *123*(7-8), 1560–1576. https://doi.org/10.1130/B30306.1

Massonnet, D., & Feigl, K. L. (1998). Radar interferometry and its application to changes in the Earth's surface. *Reviews of Geophysics*, *36*(4), 441–500. https://doi.org/10.1029/97RG03139

Mikulovsky, R.P., de la Fuente, J.A., Bell, A., Stevens, M., & Levitan, F. (2012). Activation of deep-seated landslides in NW California after wildfires in 2006 and 2008, American Geophysical Union, Fall Meeting 2012, Abstract EP13D-0878.

Mondry, Z. (2017). Sims Fire Restoration Project riparian enhancement in the Grapevine Creek Waters, in U. S. Department of Agriculture, Forest Service, Report.

Mondry, Z., & Klingel, H. (2015). Sims Fire Restoration Project Riparian #13 and #14: Roadside and Landline Fuels Reduction, in U. S. Department of Agriculture, Forest Service, Hydrology Report and Effect Analysis.

Notti, D., Herrera, G., Bianchini, S., Meisina, C., García-Davalillo, J. C., & Zucca, F. (2014). A methodology for improving landslide PSI data analysis. *International Journal of Remote Sensing*, *35*(6), 2186–2214. http://doi.org/10.1080/01431161.2014.889864

Petley, D. (2012). Global patterns of loss of life from landslides. *Geology*, *40*(10), 927–930. https://doi.org/10.1130/G33217.1

Schulz, W. H., Coe, J. A., Ricci, P. P., Smoczyk, G. M., Shurtleff, B. L., & Panosky, J. (2017). Landslide kinematics and their potential controls from hourly to decadal timescales: Insights from integrating ground-based InSAR measurements with structural maps and long-term monitoring data. *Geomorphology*, *285*, 121–136. https://doi.org/10.1016/j.geomorph.2017.02.011

Schulz, W. H., Kean, J. W., & Wang, G. (2009). Landslide movement in southwest Colorado triggered by atmospheric tides. *Nature Geoscience*, *2*(12), 863–866. https://doi.org/10.1038/ngeo659

Schulz, W. H., McKenna, J. P., Kibler, J. D., & Biavati, G. (2009). Relations between hydrology and velocity of a continuously moving landslide—Evidence of pore-pressure feedback regulating landslide motion? *Landslides*, *6*(3), 181–190. https://doi.org/10.1007/s10346-009-0157-4

Schulz, W. H., Smith, J. B., Wang, G., Jiang, Y., & Roering, J. J. (2018). Clayey landslide initiation and acceleration strongly modulated by soil swelling. *Geophysical Research Letters*, *45*, 1888–1896. https://doi.org/10.1002/2017GL076807

Shi, X., Zhang, L., Tang, M., Li, M., & Liao, M. (2017). *Landslides*, *14*(6), 1961–1973. https://doi.org/10.1007/s10346-017-0846-3

Simonett, D. S. (1967). Landslide distribution and earthquakes in the Bewani and Torricelli Mountains, New Guinea. In J. N. Jennings & J. A. Mabbutt (Eds.), *Landform Studies From Australia and New Guinea*, (pp. 64–84). New York: Cambridge University Press.

Simoni, A., Ponza, A., Picotti, V., Berti, M., & Dinelli, E. (2013). Earthflow sediment production and Holocene sediment record in a large Apennine catchment. *Geomorphology*, *188*, 42–53. https://doi.org/10.1016/j.geomorph.2012.12.006

Stimely, L. L. (2009). *Characterizing landslide movement at the Boulder creek earthflow, northern California, using L-band InSAR*, Master thesis. Eugene: University of Oregon.

Terzaghi, K. (1943). *Theoretical Soil Mechanics*. London and New York: John Wiley. https://doi.org/10.1002/9780470172766

Tofani, V., Raspini, F., Catani, F., & Casagli, N. (2013). Persistent scatterer interferometry (PSI) technique for landslide characterization and monitoring. *Remote Sensing*, *5*(3), 1045–1065. https://doi.org/10.3390/rs5031045

U.S. Department of Agriculture, Forest Service (2015). Saddle dire burned-area report (Reference FSH 2509.13).

Wasowski, J., & Bovenga, F. (2015). *Chapter 11 – Remote sensing of landslide motion with emphasis on satellite multitemporal interferometry applications: An overview, landslide hazards, risks and disasters* (pp. 345–403, ISBN 9780123964526). Amsterdam, Netherlands: Academic Press. https://doi.org/10.1016/B978-0-12-396452-6.00011-2